Long-Range Propagation and Interference of d-wave Superconducting Pairs in Graphene

D. Perconte, K. Seurre, V. Humbert, C. Ulysse, A. Sander, J. Trastoy, V. Zatko, F. Godel, P. R. Kidambi, S. Hofmann, et al.

Long-Range Propagation and Interference of d-wave Superconducting Pairs in Graphene

D. Perconte,[1,2] K. Seurre,[1] V. Humbert,[1] C. Ulysse,[3] A. Sander,[1] J. Trastoy,[1] V. Zatko,[1] F. Godel,[1] P. R. Kidambi,[4,5] S. Hofmann,[5] X. P. Zhang,[6,7] D. Bercioux,[7,8] F. S. Bergeret,[6,7] B. Dlubak,[1] P. Seneor,[1] and Javier E. Villegas[1,*]

[1] *Unité Mixte de Physique, CNRS, Thales, Université Paris-Sud, Université Paris-Saclay, 91767, Palaiseau, France*
[2] *Laboratorio de Bajas Temperaturas y Altos Campos Magnéticos, Departamento de Física de la Materia Condensada, Instituto Nicolás Cabrera and Condensed Matter Physics Center (IFIMAC), Universidad Autónoma de Madrid, E-28049 Madrid, Spain*
[3] *Centre for Nanoscience and Nanotechnology, CNRS, Université Paris-Sud/Université Paris-Saclay, Boulevard Thomas Gobert, Palaiseau, France*
[4] *Department of Chemical and Biomolecular Engineering, Vanderbilt University, 2400 Highland Avenue, Nashville, Tennessee 37212, USA*
[5] *Department of Engineering, University of Cambridge, Cambridge CB3 0FA, UK*
[6] *Centro de Física de Materiales (CFM-MPC) Centro Mixto CSIC-UPV/EHU, 20018 Donostia-San Sebastián, Basque Country, Spain*
[7] *Donostia International Physics Center, 20018 Donostia-San Sebastián, Spain*
[8] *IKERBASQUE, Basque Foundation for Science, Maria Diaz de Haro 3, 48013 Bilbao, Spain*

(Dated: September 9, 2020)

Recent experiments have shown that proximity with high-temperature superconductors induces unconventional superconducting correlations in graphene. Here we demonstrate that those correlations propagate hundreds of nanometer, allowing for the unique observation of d-wave Andreev pair interferences in $YBa_2Cu_3O_7$-graphene devices that behave as a Fabry-Pérot cavity. The interferences show as a series of pronounced conductance oscillations analogous to those originally predicted by de Gennes–Saint-James for conventional metal-superconductor junctions. The present work is pivotal to the study of exotic directional effects expected for nodal superconductivity in Dirac materials.

The superconducting proximity effect in graphene has attracted much interest since the pioneering experiments [1]. This roots down to the graphene's electronic structure, which strongly affects the underlying mechanisms: Andreev reflection and coherent propagation of electron-hole pairs [2]. A distinctive feature is the strong dependence of the proximity behavior on the graphene?s doping level, which dramatically changes the Andreev reflection [3, 4] as compared to metals. Other unique features include gate [5] or magnetic-field [6, 7] driven transitions from bulk to edge transport. Studies on graphene have also paved the way for understanding the proximity effect in other Dirac materials, such as topological insulators [8–11].

Experiments have mostly focused on conventional low critical temperature (T_C) superconductors with s-wave pairing. Despite early theoretical studies showing that d-wave (high-T_C) superconductors should lead to novel directional effects [12, 13] and exotic pairing [14, 15], evidence for unconventional superconductivity in graphene has been found only recently [16, 17]. Scanning electron tunneling microscopy (STM) of graphene on $Pr_{2-x}Ce_xCuO_4$ (PCCO) revealed a superconducting gap [16] and spectral features suggesting (p-wave) superconductivity induced in graphene. Experiments on $YBa_2Cu_3O_7$ (YBCO) and chemical-vapor-deposited (CVD) graphene devices by some of us [17] showed transparent superconductor-graphene interfaces and clear evidence of Andreev reflection. Interestingly, we also found that the Andreev electron-holes pair transmission can be modulated by a back-gate voltage, through a mechanism analogous to the Klein tunneling [18]. However, neither the STM experiments nor ours on solid-state devices probed the length scale over which the unconventional correlations penetrate into graphene.

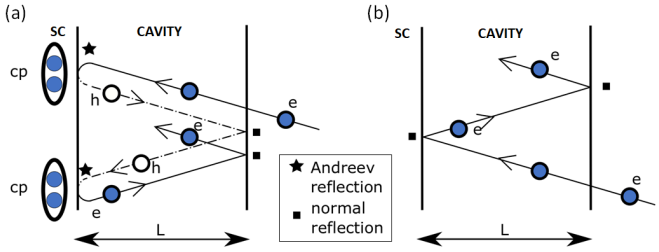

FIG. 1. Interferences in a proximitized cavity (a) An electron Andreev-reflected at the SC/cavity interface propagates as a hole back to the other end, where it is normal-reflected towards the SC/cavity interface to undergo again Andreev-reflection (AR). The lower AR is the time reversal process of the upper one. (b) The electron can also be normal-reflected at the SC/cavity, travel back to the other cavity interface to be again normal-reflected. This process results in Fabry-Pérot resonances.

Here we demonstrate the long-range propagation of

unconventional superconductivity into graphene via the observation of d-wave Andreev-pair interferences. These manifests themselves as conductance oscillations in devices that allow confining Andreev pairs within a graphene "cavity" whose length L is up to a few hundreds of nanometers. Predicted for proximitized graphene homojunctions [12, 13], the oscillations are analogous to the de Gennes–Saint-James [19] and McMillan–Rowel resonances [20] in the electronic density of states of ultrathin normal-metals backed by superconductors. Figure 1(a) displays a cartoon of the underlying mechanism. Electrons injected in the cavity are Andreev-reflected as holes at the interface with the superconductor, retrace their path to the opposite cavity's end where they are normal-reflected, and travel bain ck towards the superconductor, where they are again Andreev-reflected (now as electrons). This results in destructive/constructive interferences dictated by the energy-dependent phase accumulated along the loop. This phenomenon shows up as conductance oscillations as a function of the bias voltage $V_{\rm BIAS}$. Because Andreev pairs stemming from YBCO have d-wave symmetry, they decay over distances comparable to the mean free path l [21, 22], the observation of Andreev-pair interferences implies ballistic or quasi-ballistic transport. Consistently, the Andreev-pair interferences are accompanied by normal-electron resonances that result from normal-reflections at the two cavity's ends [sketch in Fig. 1(b)] and commensurability between L and the electrons' wavelength [18, 23–26]. These different resonances result in oscillations as a function of both the gate V_G and bias $V_{\rm BIAS}$, and can be distinguished from Andreev-pairs related ones by their distinct periodicity and voltage regime in which they dominate. To our knowledge, the concurrent observation of both resonances had been restricted to junctions between s-wave superconductors and topological insulators [9, 10], in which Andreev-pair interferences manifest at very low-temperatures as a function of the gate voltage V_G . Here they can be observed at higher temperatures and show in a rich series of oscillations as a function of $V_{\rm BIAS}$ because of the high-$T_{\rm C}$ and large gap of YBCO (tens of meV) which, contrary to low-temperature superconductors [27], may enclose many orders of interference.

The planar devices [Fig. 2(a)] consist of four superconducting (SC) c-axis oriented $\rm YBCO_{50nm}/Au_{4nm}$ electrodes disposed within an insulating (INS) YBCO matrix and separated by a gap of length 100 nm$< L <$ 800 nm. As-grown YBCO films showed $T_{\rm C} \sim 90$ K while $T_{\rm C} \sim 70$ K for lithographed devices, indicating moderate deoxygenation during fabrication. The ultrathin Au interlayer is deposited *in situ* to preserve the superconducting properties and improve the interfacial transparency [17]. The Au interlayer is crucial: none of the effects reported here could be observed in its absence. Notice that the Au layer thickness it is one order of magnitude thinner than the mean free path in Au, and consequently d-wave correlations expectedly propagate undisturbed across it [21, 22]. A single-layer CVD grown [28] graphene bridge (G) connects the four electrodes, each of which terminates in a gold pad [1-4 in Fig. 2(b)] used for wire-bonding. The transparency of the electrical contact between each SC electrode and the graphene varied largely, even within a single device. Here we report on effects that arise only at high transparency contacts, which is often the case for just one out of four contacts per device. The structure is covered by a 45 nm thick AlO_x layer (gate dielectric) [29]. As reported earlier [30], with this encapsulation the carrier mobility in the used CVD graphene reaches up to $\mu \sim 7000$ cm^2 V^{-1}s^{-1}. The top-gate is made of Au entirely [Fig. 2(c)] and the gate capacitance as measured over insulating YBCO is $C_G \sim 5 \times 10^{11} e$ cm^{-2} V^{-1} (with e the electron charge). Further details are reported elsewhere [17].

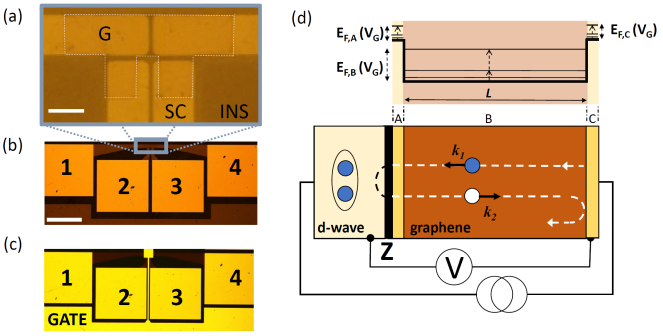

FIG. 2. Micrograph of a graphene/YBCO superconducting device. The scale bar is 10 μm. (a) shows a zoom on the junction: Superconducting electrodes (SC) are connected by graphene bridges (G) on top of insulating YBCO (INS). The scale bar is 100 μm. (c) Micrograph of a device with the top gate. (d) Scheme of the graphene homojunction model. The doping depends on whether graphene lies on insulating or superconducting YBCO, which results in three graphene regions A B, C with different Fermi energy. This creates the cavity where interferences occur. The lower scheme shows the equivalent electrical circuit. The YBCO-Au-graphene interface, characterized by a barrier strength Z, is measured in series with the cavity.

We performed three-probe measurements, with the current I injected *e.g.* from 1 to contact 4 and the $V_{\rm BIAS}$ measured between 1 and 3. Thus we probe the YBCO-Au-graphene interface in series with the graphene "cavity" formed between the SC electrodes, as sketched in in Fig. 2(d). The wiring as well as Au/YBCO contact resistances are Ohmic and negligible [17]. The differential conductance $G(V_{\rm BIAS}) = dI/dV_{\rm BIAS}$ is measured using a Keithley 6221 current source coupled to a Keithley 2182.

Examples of low-temperature (3.2 K) differential conductance measurements are shown in Fig. 3(a), 3(d) and Fig. 4(a). The differential conductance $G(V_{\rm BIAS})$ shows a low-bias feature that stands out from the high-bias conductance level. That is either a conductance decrease

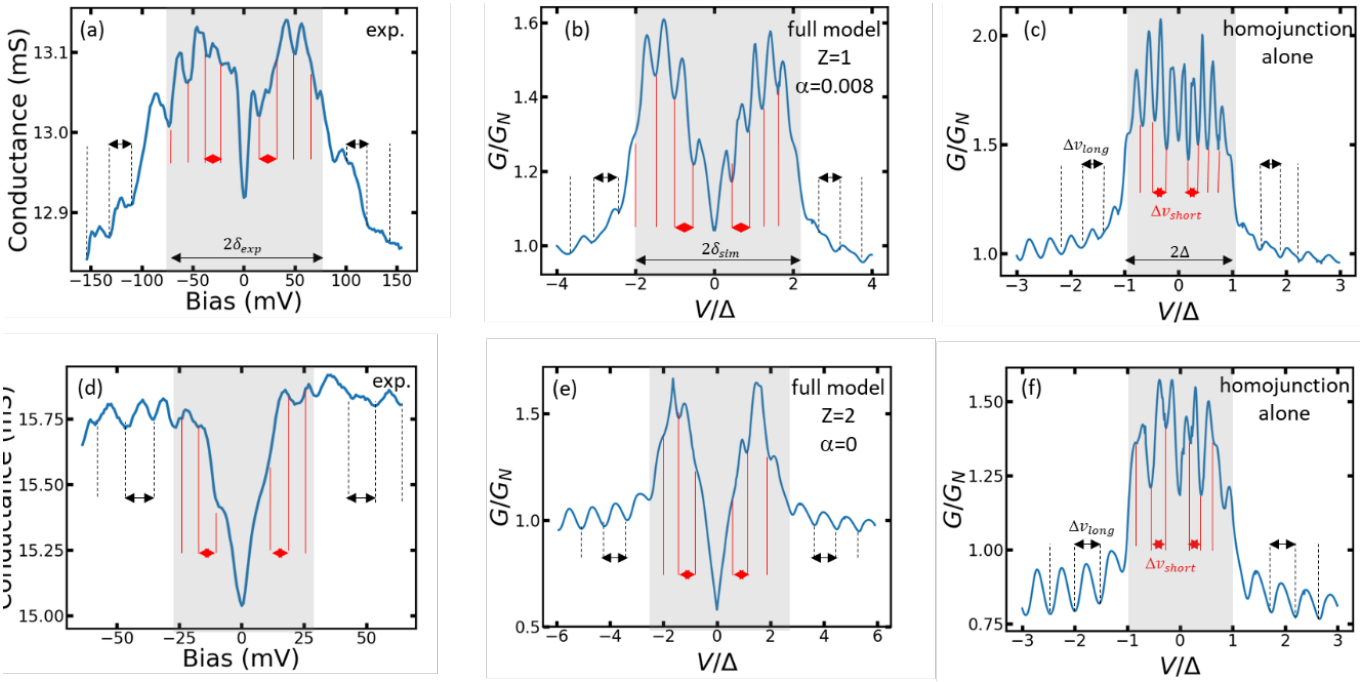

FIG. 3. Conductance versus $V_{\rm BIAS}$ for two different devices, B3U (a) and B4U (b) measured at 3.2 K. Vertical lines point out the series of oscillations, and the horizontal double-headed arrows indicate the periods $V_{\rm long}$ (black) and $V_{\rm short}$ (red). The shaded area indicates the width 2δ of the superconducting-gap related feature. (b) and (e) show corresponding full-model calculations of the conductance with the Z and indicated in the legend (c) and (f) shows simulations for a proximitized graphene cavity alone, without finite-Z junction in series.

[Fig. 3(d)] or an enhancement [Fig. 4(a)] within a typical bias range $|V_{\rm BIAS}| < \delta_{\rm exp} \sim 20-70$ mV highlighted by the grey shade. Those features are reminiscent of the conductance decrease/increase observed for $e|V_{\rm BIAS}| < \Delta$ in superconducting/normal-metal junctions depending on the interface transparency [31]. However, here they extend over a bias range $\delta_{\rm exp}$ that clearly exceeds the superconducting energy-gap expected for moderately-underdoped to optimally-doped YBCO, which is reported in the range $\Delta_{\rm YBCO} \sim 15-30$ meV [32–35]. Furthermore, details such as the sharp zero-bias peak observed for some devices (see *e.g.* B4D and E3D in the Supplemental Material [36]) are characteristic of junctions involving d-wave superconductors, and appear when the d-wave nodes form a certain angle with respect to the junction interface [33, 37, 38].

In addition to the central features, an oscillation pattern appears in Fig. 3(a) and 3(d), this extends over a bias range well above $\delta_{\rm exp}$. Indeed, two types of oscillations exist: the ones with longer period $V_{\rm long}$, predominant for $|V_{\rm BIAS}| > \delta_{\rm exp}$, and the other with shorter $V_{\rm short}$ which are more prominent at $|V_{\rm BIAS}| < \delta_{\rm exp}$.

Figure 4 show an example of gating effects. Figure 4(a) displays $G(V_{\rm BIAS})$ without gate voltage ($V_G = 0$), and shows the general features discussed above. Figure 4(b) is a color plot of a series of $G(V_{\rm BIAS})$ at constant temperature and varying V_G. The central (red) feature corresponds to the zero-bias conductance peak. The conductance is periodically modulated by V_G: a pattern of oblique lines (light-blue/green) indicates that V_G gradually "shifts" the oscillations observed as a function of $V_{\rm BIAS}$. The oblique lines' slope gradually varies with V_G, which results in pronounced curvature over the plot periphery (low V_G or high $|V_{\rm BIAS}|$).

We discuss now a model that explains the main observations, namely (i) the increase or decrease of the zero-bias conductance; (ii) the origin and period of conductance oscillations. The model is based on the Blonder-Tinkham-Klapwijk (BTK) formalism [31] extended to junctions between d-wave superconductors and normal metals [39] and to proximitized graphene homojunctions [12, 13]. A scheme is shown in Fig. 2(d). First, we consider the YBCO-Au-graphene interface. Because the Au thickness (~ 5 nm) is well-below the mean free path $l_{\rm Au} \sim 40$ nm [40] and the low-T coherence length $\xi_{\rm Au} = v_F l/(6\pi KT) \sim 30$ nm [41], we characterize that interface [black in Fig. 2(d)] via a single Blonder-Tinkham-Klapwijk barrier-strength parameter Z. If $Z = 0$, the transmission between YBCO and graphene is only mediated by the Andreev reflection. By increasing Z, Andreev reflection turns less dominant, normal reflection is enhanced, and transmission is dominated by tunneling. We model the graphene "channel" where Andreev pairs and normal electrons propagate, considering three different

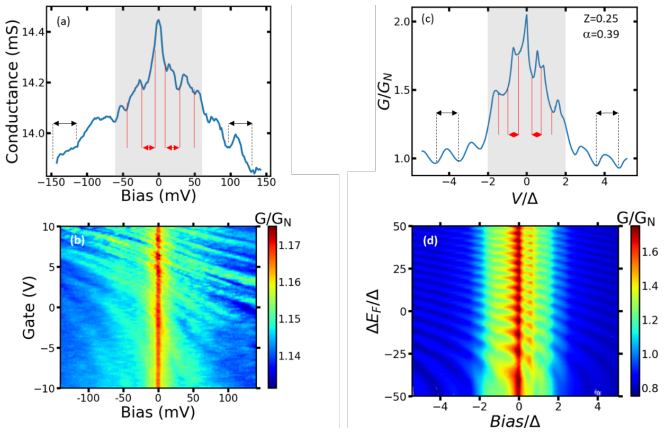

FIG. 4. (a) Conductance versus $V_{\rm BIAS}$ for device A5U, measured at $T = 4$ K. (b) Same device conductance (color scale) as function of bias voltage (horizontal axis) and gate voltage (vertical axis). (c) Full-model calculation of the conductance with Z and α indicated in the legend. (d) corresponding full-model calculation of the conductance as a function of bias and the Fermi energy variation in the cavity.

regions A, B, C. A and C correspond to graphene lying on superconducting YBCO/Au [yellow in Fig. 2(d)], but we consider that only contact A has a relatively low Z. The region B of length L [dark in Fig. 2(d)] lies on insulating YBCO. Here the Fermi energy $E_{F,B}$ is expectedly different from $E_{F,A}$, $E_{F,C}$ as the graphene's doping depends on the substrate's electronic properties [42]. Within this model, the structure is a graphene homojunction with a gate-tunable Fermi energy step, as sketched in the upper Fig. 2(d), and behaves as a resonant cavity for electrons and Andreev pairs.

The conductance is calculated numerically by considering the YBCO-Au-graphene interface [33, 39] and the proximitized graphene homojunction [12, 13] in-series (see Supplemental Material for details [36]). The input parameters are Z, the reduced Fermi energies $\epsilon_{F,i} \equiv E_{F,i}/\Delta$ (with $i =$ A, B, C and Δ the energy-gap induced in A by proximity effect), the reduced cavity's length $\Lambda \equiv L/\lambda_{F,A}$ (with the Fermi wavelength $\lambda_{F,A}$, chosen as a reference following the original model [12, 13]), and α the effective angle between d-wave anti-nodes and the homojunction interfaces. The key parameters are Λ and $\epsilon_{F,A}$: they determine $V_{\rm long}$ and $V_{\rm short}$. The parameters α and Z determine the conductance background shape, and particularly whether there is a conductance decrease or enhancement around zero bias. We stress that the sharp zero-bias peak observed in some devices cannot be reproduced by the simulation unless we consider $\alpha \neq 0$ (see Supplemental Material [36] Sec. 7). This is a consequence of the d-wave symmetry of the correlations propagating across the different interfaces. The parameters $\epsilon_{F,B}$ and $\epsilon_{F,C}$ only change the oscillations' phase and amplitude, but do not affect their period [13]. To choose the simulation parameters that yield the best agreement with the experimental curves we proceed as detailed in the Supplemental Material in Sec. 2-4 [36]. Simulations examples are shown in Fig. 3(b), 3(e) and Fig. 4(c) for the experiments in Fig. 3(a), 3(d) and Fig. 4(a), respectively. The simulations closely reproduce the main experimental features [further examples and the simulations' parameters shown in the Supplemental Material [36] in Secs. 5 and 6].

In order to illustrate the different contributions to the conductance, Figs. 3(c) and 3(f) display the conductance of a proximitized graphene homojunction [13] alone, *i.e.* without a finite-Z junction in series. The same $\epsilon_{F,i}$, Λ and α as for the full-model calculations are used. Here the conductance shows a background dependence on $V_{\rm BIAS}$ very different from the experiments, which evidences that it is strongly influenced by the YBCO-Au-graphene interface. In particular, the zero-bias "dip" only emerges if a finite-Z junction is considered. However, Figs. 3(c) and 3(f) do show the short and long period oscillations observed experimentally. This demonstrates that they originate within the graphene homojunction. Notice that the ratio between the short and long periods is different from that in the experiments (and full model simulations): in Fig. 3(c) and 3(f), $V_{\rm short}$ is clearly shorter (relative to $V_{\rm long}$) than in Fig. 3(a)-3(b) and 3(d)-3(e). This is because in experiments (and full-model) $V_{\rm BIAS}$ is divided between the graphene homojunction and the YBCO-Au-graphene interface, and the strongly non-linear conductance leads to a voltage distribution that varies depending on the $V_{\rm BIAS}$. In particular, for $eV_{\rm BIAS} < \Delta$ the conductance across the YBCO-Au-graphene interface decreases (this is more pronounced for higher Z values) while the homojunction conductance increases [see Figs. 3(c), 3(f)]. Consequently, $V_{\rm short}$ (observed for $eV_{\rm BIAS} < \Delta$) appears "stretched" relative to the $V_{\rm long}$ (observed for $eV_{\rm BIAS} > \Delta$).

The oscillations' physical meaning can be understood from Fig. 5. This displays the short (red circles) and long (black squares) oscillation periods as a function of the inverse of the cavity length $L_{\rm device}^{-1}$ defined upon devices fabrication. Specifically, we plot the period $V = v\Delta$, where Δ is estimated as discussed in the Supplemental Material [36] and v is the period obtained from our model once the contribution of the YBCO-Au-graphene interface has been removed — as in Fig. 3(c) and 3(e) — to avoid the aforementioned $V_{\rm BIAS}$ division artifacts.

The long-period oscillations follow $V_{\rm th,\,long} = hv_F/2L_{\rm device}$. This is as expected from the interference between electrons travelling back and forth from one cavity side to the other after normal reflections [Fig. 1(b)]. This period results [5, 18, 23–25] from the interference condition $2L_{\rm device}k = 2n\pi$ (with n an integer and k the electron wavevector) and the graphene's linear dispersion, which yields $V = \hbar v_F k$ [43]. These interferences imply normal-electron coherence over $\sim L_{\rm device}$. Their

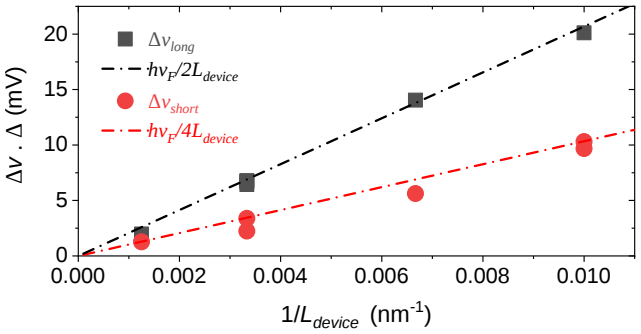

FIG. 5. Oscillations period as a function of the cavity length L_{device}. The black and red dashed lines respectively correspond to the period theoretically expected for electron (Fabry-Pérot) and Andreev-pair (De Gennes-Saint James) interferences.

amplitude is greater for 100 nm $< L_{\text{device}} <$ 300 nm but drastically diminishes beyond that. This suggests that the mean free path is above 100 nm but clearly below 1 μm, in agreement with a rough estimate based on the carrier mobility [44] which yields $l \lesssim 100 - 260$ nm . Notice that the scaling of the period with $1/L_{\text{device}}$ rules out Tomasch resonances [45–47] within YBCO, which should scale with its thickness and should therefore show the same period for all devices.

The short period oscillations, clearly visible for $V < \Delta$, follow $V_{th,short} = hv_F/4L_{\text{device}}$. This period is expected from the interference of Andreev pairs [19, 20] — scheme in Fig. 1(a). In this case the resonance condition reads $2L_{\text{device}}|k_1 - k_2| = 2n\pi$, where k_1 and k_2 are the electron and reflected hole wavevectors, whose difference is established by the applied voltage $|k_1 - k_2| = 2V/\hbar v_F$ [20]. These resonances imply that the superconducting coherence is preserved over $\sim L_{\text{device}}$.

Our model also explains the gating effects. Figure 4(d) displays a simulated conductance as a function of bias and Fermi energy, which reproduces the main experimental features — particularly the pattern of oblique lines that characterize the conductance modulation by by V_G [Fig.4(b)]. The correspondence between the y-axis in simulations and experiments implies that the Fermi energy (and vector k_F) is varied about proportionally to V_G, in agreement with earlier experiments [17]. Varying k_F produces a periodic modulation of the conductance, via the resonance condition $2L_{\text{device}}k_F = 2n\pi$, yielding the oblique lines. Note that the model also reproduces the slope gradual change, and the pronounced curvature over the plot's periphery, which is obtained by including in the model $\epsilon_{F,B}(V_G) \neq \epsilon_{F,A}(V_G) = \epsilon_{F,C}(V_G)$ to account for a partial pining of graphene Fermi energy on conducting YBCO.

In summary, we have realized ballistic planar devices in which graphene is proximitized by a d-wave cuprate superconductor. We find that the d-wave correlations propagate into graphene over hundreds of nanometers at ~ 4 K. The confinement of Andreev pairs and electrons in graphene homojunctions of submicrometric lateral dimensions produces quantum interferences that show as conductance oscillations. Those involving Andreev pairs, more prominent below the superconducting gap, are analogous to the De Gennes-Saint James oscillations. Although difficult to observe in graphene/low-temperature superconductor devices, here they are very clear due to the large YBCO gap (tens of mV), which fits many orders of interference within. The unusual d-wave Andreev-pair interferences are accompanied by normal-electron ones. The simultaneous observation of both is rare, and stems from the fact that the coherence length of d-wave correlations is limited by the mean free path [22]. Thus, the necessary condition for both types of resonances is satisfied simultaneously here. Extensions of this study to graphene with lower intrinsic doping and higher carrier mobility should allow exploring specular Andreev reflection regimes [3] rand Josephson effects. The latter would also require enhancing the transparency of the graphene/YBCO interface, possibly by replacing the Au interlayer, in order to routinely obtain low-Z junctions. Further, perspectives include novel directional effects [14, 15] linked to the d-wave character of the induced correlations, which could be exploited in more sophisticated devices to realize topological states [48]. This work should also further encourage studies in which graphene is replaced by other 2D materials with intrinsically interesting proximity behavior [49, 50], eventually combined with exfoliated d-wave superconductors [51].

Work at Unité Mixte de Physique CNRS/Thales supported by the ERC Grant No. 647100 "SUSPINTRONICS", French ANR Grants No. ANR-15-CE24-0008-01 "SUPERTRONICS" and No. ANR-17-CE30-0018-04 "OPTOFLUXONICS", Labex NanoSaclay No. ANR-10-LABX-0035, European COST action 16218 "Nanocohybri" , and EU Work Programme Graphene Flagship (Grants No. 696656 and 785219). This work was supported by the French RENATECH network (French national nanofabrication platform). X.P.Z., D.B., and F.S.B. acknowledge support from Ministerio de Ciencia e Innovacion (MICINN) through Project No. FIS2017-82804-P. F. S. B. acknowledges Grupos Consolidados UPV/EHU del Gobierno Vasco (Grant No. IT1249- 19). We thank Professor. J. Santamaría for discussions.

* javier.villegas@cnrs-thales.fr

[1] Hubert B. Heersche, Pablo Jarillo-Herrero, Jeroen B. Oostinga, Lieven M. K. Vandersypen, and Alberto F. Morpurgo, "Bipolar supercurrent in graphene," Nature **446**, 56–59 (2007).

[2] T. M. Klapwijk, "Proximity effect from an andreev perspective," Journal of Superconductivity **17**, 593–611

(2004).
[3] C. W. J. Beenakker, "Specular andreev reflection in graphene," Phys. Rev. Lett. **97**, 067007 (2006).
[4] D. K. Efetov, L. Wang, C. Handschin, K. B. Efetov, J. Shuang, R. Cava, T. Taniguchi, K. Watanabe, J. Hone, C. R. Dean, and P. Kim, "Specular interband Andreev reflections at van der Waals interfaces between graphene and $NbSe_2$," Nature Physics **12**, 328–332 (2015).
[5] M. T. Allen, O. Shtanko, I. C. Fulga, A. R. Akhmerov, K. Watanabe, T. Taniguchi, P. Jarillo-Herrero, L. S. Levitov, and A. Yacoby, "Spatially resolved edge currents and guided-wave electronic states in graphene," Nature Physics **12**, 128–133 (2015).
[6] M. Ben Shalom, M. J. Zhu, V. I. Fal'ko, A. Mishchenko, A. V. Kretinin, K. S. Novoselov, C. R. Woods, K. Watanabe, T. Taniguchi, A. K. Geim, and J. R. Prance, "Quantum oscillations of the critical current and high-field superconducting proximity in ballistic graphene," Nature Physics **12**, 318–322 (2015).
[7] F. Amet, C. T. Ke, I. V. Borzenets, J. Wang, K. Watanabe, T. Taniguchi, R. S. Deacon, M. Yamamoto, Y. Bomze, S. Tarucha, and G. Finkelstein, "Supercurrent in the quantum hall regime," Science **352**, 966–969 (2016).
[8] Gad Koren, Tal Kirzhner, Yoav Kalcheim, and Oded Millo, "Signature of proximity-induced $p_x + ip_y$ triplet pairing in the doped topological insulator Bi_2Se_3 by the s-wave superconductor NbN," EPL (Europhysics Letters) **103**, 67010 (2013).
[9] A. D. K. Finck, C. Kurter, Y. S. Hor, and D. J. Van Harlingen, "Phase coherence and andreev reflection in topological insulator devices," Phys. Rev. X **4**, 041022 (2014).
[10] A. D. K. Finck, C. Kurter, E. D. Huemiller, Y. S. Hor, and D. J. Van Harlingen, "Robust Fabry-Pérot interference in dual-gated Bi_2Se_3 devices," Applied Physics Letters **108**, 203101 (2016).
[11] Erwann Bocquillon and Russell S. Deacon and Jonas Wiedenmann and Philipp Leubner and Teunis M. Klapwijk and Christoph Brüne and Koji Ishibashi and Hartmut Buhmann and Laurens W. Molenkamp, "Gapless andreev bound states in the quantum spin hall insulator HgTe," Nature Nanotechnology **12**, 137–143 (2016).
[12] J. Linder and A. Sudbø, "Dirac fermions and conductance oscillations in s- and d-wave superconductor-graphene junctions," Phys. Rev. Lett. **99**, 147001 (2007).
[13] Jacob Linder and Asle Sudbø, "Tunneling conductance in s- and d-wave superconductor-graphene junctions: Extended Blonder-Tinkham-Klapwijk formalism," Phys. Rev. B **77**, 064507 (2008).
[14] Jacob Linder, Annica M. Black-Schaffer, Takehito Yokoyama, Sebastian Doniach, and Asle Sudbø, "Josephson current in graphene: Role of unconventional pairing symmetries," Phys. Rev. B **80**, 094522 (2009).
[15] Oladunjoye A. Awoga and Annica M. Black-Schaffer, "Probing unconventional superconductivity in proximitized graphene by impurity scattering," Phys. Rev. B **97**, 214515 (2018).
[16] A. Di Bernardo, O. Millo, M. Barbone, H. Alpern, Y. Kalcheim, U. Sassi, A. K. Ott, D. De Fazio, D. Yoon, M. Amado, A. C. Ferrari, J. Linder, and J. W. A. Robinson, "p-wave triggered superconductivity in single-layer graphene on an electron-doped oxide superconductor," Nature Communications **8**, 14024 (2017).
[17] David Perconte, Fabian A. Cuellar, Constance Moreau-Luchaire, Maelis Piquemal-Banci, Regina Galceran, Piran R. Kidambi, Marie-Blandine Martin, Stephan Hofmann, Rozenn Bernard, Bruno Dlubak, Pierre Seneor, and Javier E. Villegas, "Tunable Klein-like tunnelling of high-temperature superconducting pairs into graphene," Nature Physics **14**, 25–29 (2017).
[18] Andrea F. Young and Philip Kim, "Quantum interference and Klein tunnelling in graphene heterojunctions," Nature Physics **5**, 222–226 (2009).
[19] P.G. de Gennes and D. Saint-James, "Elementary excitations in the vicinity of a normal metal-superconducting metal contact," Physics Letters **4**, 151–152 (1963).
[20] J. M. Rowell and W. L. McMillan, "Electron interference in a normal metal induced by superconducting contracts," Physical Review Letters **16**, 453–456 (1966).
[21] Toshihiko Tsuneto, "On dirty superconductors," Progress of Theoretical Physics **28**, 857–869 (1962).
[22] A. V. Balatsky, I. Vekhter, and Jian-Xin Zhu, "Impurity-induced states in conventional and unconventional superconductors," Reviews of Modern Physics **78**, 373–433 (2006).
[23] Wenjie Liang, Marc Bockrath, Dolores Bozovic, Jason H. Hafner, M. Tinkham, and Hongkun Park, "Fabry-Pérot interference in a nanotube electron waveguide," Nature **411**, 665–669 (2001).
[24] F. Miao, S. Wijeratne, Y. Zhang, U. C. Coskun, W. Bao, and C. N. Lau, "Phase-coherent transport in graphene quantum billiards," Science **317**, 1530–1533 (2007).
[25] L.C. Campos, A.F. Young, K. Surakitbovorn, K. Watanabe, T. Taniguchi, and P. Jarillo-Herrero, "Quantum and classical confinement of resonant states in a trilayer graphene Fabry-Pérot interferometer," Nature Communications **3**, 1239 (2012).
[26] Monica T. Allen, Oles Shtanko, Ion C. Fulga, Joel I.-J. Wang, Daniyar Nurgaliev, Kenji Watanabe, Takashi Taniguchi, Anton R. Akhmerov, Pablo Jarillo-Herrero, Leonid S. Levitov, and Amir Yacoby, "Observation of Electron Coherence and Fabry-Pérot Standing Waves at a Graphene Edge," Nano Letters **17**, 7380–7386 (2017).
[27] Francesco Giazotto, Pasqualantonio Pingue, Fabio Beltram, Marco Lazzarino, Daniela Orani, Silvia Rubini, and Alfonso Franciosi, "Resonant Transport in Nb /GaAs /AlGaAs Heterostructures: Realization of the de Gennes–Saint-James Model," Phys. Rev. Lett. **87**, 216808 (2001).
[28] Piran R. Kidambi, Caterina Ducati, Bruno Dlubak, Damian Gardiner, Robert S. Weatherup, Marie-Blandine Martin, Pierre Seneor, Harry Coles, and Stephan Hofmann, "The Parameter Space of Graphene Chemical Vapor Deposition on Polycrystalline Cu," The Journal of Physical Chemistry C **116**, 22492–22501 (2012).
[29] B. Dlubak, P. R. Kidambi, R. S. Weatherup, S. Hofmann, and J. Robertson, "Substrate-assisted nucleation of ultra-thin dielectric layers on graphene by atomic layer deposition," Applied Physics Letters **100**, 173113 (2012).
[30] S. Mzali, A. Montanaro, S. Xavier, B. Servet, J.-P. Mazellier, O. Bezencenet, P. Legagneux, M. Piquemal-Banci, R. Galceran, B. Dlubak, P. Seneor, M.-B. Martin, S. Hofmann, J. Robertson, C.-S. Cojocaru, A. Centeno, and A. Zurutuza, "Stabilizing a graphene platform toward discrete components," Applied Physics Letters **109**, 253110 (2016).
[31] G. E. Blonder, M. Tinkham, and T. M. Klapwijk, "Transition from metallic to tunneling regimes in supercon-

ducting microconstrictions: Excess current, charge imbalance, and supercurrent conversion," Physical Review B **25**, 4515–4532 (1982).

[32] I. Maggio-Aprile, Ch. Renner, A. Erb, E. Walker, and Ø. Fischer, "Direct Vortex Lattice Imaging and Tunneling Spectroscopy of Flux Lines on $YBa_2Cu_3O_{7-\delta}$," Phys. Rev. Lett. **75**, 2754–2757 (1995).

[33] J. Y. T. Wei, N.-C. Yeh, D. F. Garrigus, and M. Strasik, "Directional Tunneling and Andreev Reflection on $YBa_2Cu_3O_{7-\delta}$ Single Crystals: Predominance of d-Wave Pairing Symmetry Verified with the Generalized Blonder, Tinkham, and Klapwijk Theory," Phys. Rev. Lett. **81**, 2542–2545 (1998).

[34] Y. Dagan, R. Krupke, and G. Deutscher, "Determination of the superconducting gap in $YBa_2Cu_3O_{7-\delta}$ by tunneling experiments under magnetic fields," Phys. Rev. B **62**, 146–149 (2000).

[35] V. Rouco, R. El Hage, A. Sander, J. Grandal, K. Seurre, X. Palermo, J. Briatico, S. Collin, J. Trastoy, K. Bouzehouane, A. I. Buzdin, G. Singh, N. Bergeal, C. Feuillet-Palma, J. Lesueur, C. Leon, M. Varela, J. Santamaría, and Javier E. Villegas, "Quasiparticle tunnel electroresistance in superconducting junctions," Nature Communications **11**, 658 (2020).

[36] See Supplemental Material at [url] for: I. Theoretical model, II. Simulation procedure, III. Variability of the fitting parameters, IV. Quantitative evaluation of the simulation parameters, V. Table of simulation parameters, VI. Simulation vs. experiment for the set of devices, VII. Induced superconducting correlations: d-wave versus s-wave.

[37] Satoshi Kashiwaya, Yukio Tanaka, Masao Koyanagi, Hiroshi Takashima, and Koji Kajimura, "Origin of zero-bias conductance peaks in high-T_c superconductors," Phys. Rev. B **51**, 1350–1353 (1995).

[38] Amos Sharoni, Itay Asulin, Gad Koren, and Oded Millo, "Proximity Effect in Gold-Coated $YBa_2Cu_3O_{7-\delta}$ Films Studied by Scanning Tunneling Spectroscopy," Phys. Rev. Lett. **92**, 017003 (2004).

[39] Satoshi Kashiwaya, Yukio Tanaka, Masao Koyanagi, and Koji Kajimura, "Theory for tunneling spectroscopy of anisotropic superconductors," Physical Review B **53**, 2667–2676 (1996).

[40] E. Scheer, W. Belzig, Y. Naveh, M. H. Devoret, D. Esteve, and C. Urbina, "Proximity effect and multiple andreev reflections in gold atomic contacts," Physical Review Letters **86**, 284–287 (2001).

[41] Amos Sharoni, Itay Asulin, Gad Koren, and Oded Millo, "Proximity Effect in Gold-Coated $YBa_2Cu_3O_{7-\delta}$ Films Studied by Scanning Tunneling Spectroscopy," Phys. Rev. Lett. **92**, 017003 (2004).

[42] Choongyu Hwang, David A. Siegel, Sung-Kwan Mo, William Regan, Ariel Ismach, Yuegang Zhang, Alex Zettl, and Alessandra Lanzara, "Fermi velocity engineering in graphene by substrate modification," Scientific Reports **2**, 590 (2012).

[43] A. H. Castro Neto, F. Guinea, N. M. R. Peres, K. S. Novoselov, and A. K. Geim, "The electronic properties of graphene," Reviews of Modern Physics **81**, 109–162 (2009).

[44] E. H. Hwang and S. Das Sarma, "Acoustic phonon scattering limited carrier mobility in two-dimensional extrinsic graphene," Phys. Rev. B **77**, 115449 (2008).

[45] W. J. Tomasch, "Geometrical resonance and boundary effects in tunneling from superconducting in," Physical Review Letters **16**, 16–19 (1966).

[46] O. Nesher and G. Koren, "Observation of tomasch oscillations and tunneling-like behavior in oxygen-deficient edge junctions," Applied Physics Letters **74**, 3392–3394 (1999).

[47] C. Visani, Z. Sefrioui, J. Tornos, C. Leon, J. Briatico, M. Bibes, A. Barthélémy, J. Santamaría, and Javier E. Villegas, "Equal-spin andreev reflection and long-range coherent transport in high-temperature superconductor/half-metallic ferromagnet junctions," Nature Physics **8**, 539–543 (2012).

[48] P. Lucignano, F. Tafuri, and A. Tagliacozzo, "Topological rf squid with a frustrating π junction for probing the majorana bound state," Phys. Rev. B **88**, 184512 (2013).

[49] Dushko Kuzmanovski, Jacob Linder, and Annica Black-Schaffer, "Quantum ground state control in superconductor-silicene structures: 0-π transitions, φ_0-junctions, and majorana bound states," Phys. Rev. B **94**, 180505 (2016).

[50] Jacob Linder and Takehito Yokoyama, "Anisotropic andreev reflection and josephson effect in ballistic phosphorene," Physical Review B **95**, 144515 (2017).

[51] Ang J. Li, Xiaochen Zhu, G. R. Stewart, and Arthur F. Hebard, "Bi-2212/1T-TaS_2 Van der Waals junctions: Interplay of proximity induced high-T c superconductivity and CDW order," Scientific Reports **7**, 4639 (2017).

Supplemental Material: Long-Range Propagation and Interference of d-wave Superconducting Pairs in Graphene

D. Perconte,[1,2] K. Seurre,[1] V. Humbert,[1] C. Ulysse,[3] A. Sander,[1] J. Trastoy,[1] V. Zatko,[1] F. Godel,[1] P. R. Kidambi,[4,5] S. Hofmann,[5] X. P. Zhang,[6,7] D. Bercioux,[7,8] F. S. Bergeret,[6,7] B. Dlubak,[1] P. Seneor,[1] and Javier E. Villegas[1,*]

[1] *Unité Mixte de Physique, CNRS, Thales, Université Paris-Sud, Université Paris-Saclay, 91767, Palaiseau, France*

[2] *Laboratorio de Bajas Temperaturas y Altos Campos Magnéticos, Departamento de Física de la Materia Condensada, Instituto Nicolás Cabrera and Condensed Matter Physics Center (IFIMAC), Universidad Autónoma de Madrid, E-28049 Madrid, Spain*

[3] *Centre for Nanoscience and Nanotechnology, CNRS, Université Paris-Sud/Université Paris-Saclay, Boulevard Thomas Gobert, Palaiseau, France*

[4] *Department of Chemical and Biomolecular Engineering, Vanderbilt University, 2400 Highland Avenue, Nashville, Tennessee 37212, USA*

[5] *Department of Engineering, University of Cambridge, Cambridge CB3 0FA, UK*

[6] *Centro de Física de Materiales (CFM-MPC) Centro Mixto CSIC-UPV/EHU, 20018 Donostia-San Sebastián, Basque Country, Spain*

[7] *Donostia International Physics Center, 20018 Donostia-San Sebastián, Spain*

[8] *IKERBASQUE, Basque Foundation for Science, Maria Diaz de Haro 3, 48013 Bilbao, Spain*

(Dated: September 9, 2020)

CONTENTS

* javier.villegas@cnrs-thales.fr

I. THEORETICAL MODEL

We reproduce the experimental device conductance via numerical simulations based on combination of the models of Refs. [1] and [2]. The model of Ref. [1] applies to a graphene homojunction proximitized by a d-wave superconductor. The junction is divided into three different sections A, B, C connected in series. Each of them has a different Fermi energy and together form an energy quantum well which is tuneable upon application of a gate voltage (in the case studied here, we assume that the different gate capacitance on insulating and metallic YBCO lead to different gating effects in A, C and B). In order to allow for Andreev reflection at the A/B interface, the model [1] assumes that the electronic density of states in region A presents a superconducting energy-gap. The homostructure conductance is obtained by matching the electronic wave functions in the A/B and C/B interfaces. Given the transmission $T = \left(1 - |r|^2\right)$ and reflection $R = |r_A|^2$ coefficient, the full expressions for r and r_A are cumbersome and can be found in the appendix of Ref. [3]. The conductance across the A/B/C structure is given by:

$$G_1\left(V_1\right) = \int_{-\frac{\pi}{2}}^{\frac{\pi}{2}} d\theta \left(1 - |r|^2\right) \cos\left(\theta\right) + |r_A|^2 \cos\left(\theta_A\right). \tag{SE1}$$

With $\theta_A = \arcsin\left[\left(eV_1 + E_f\right) / \left(eV_1 - E_f\right) \sin\left(\theta\right)\right]$ and θ the electron angle of incidence with respect to the interfaces. Both r and r_A and thus the conductance $G_1(V_1)$ depend on the following parameters: the reduced channel length $\Lambda \equiv L/\lambda_{F,A}$ (with $\lambda_{F,A}$ the Fermi wavelength in A), the reduced graphene Fermi energy in the different regions ($\epsilon_{F,i} \equiv E_{F,i}/\Delta$, with i=A, B, C) and Δ the amplitude of the superconducting energy-gap, and the angle between the d-wave nodes of the superconducting order parameter and the interface α. The model makes a full wave matching calculation such that effects coming from different angles of incidence after several reflections are taken into account. As discussed in the manuscript, this first block of the model explains the conductance oscillations as a function of gate and bias voltage. It is important to notice that the above result applies to electrons that propagate ballistically within the B-region.

The second block of the model takes into account the finite transmission of the YBCO/Au/graphene interface that is model as a d-wave/metal interface as studied in Refs. [2] and [4]. Specifically, the conductance is given by:

$$G_2\left(V_2\right) = \int_{-\frac{\pi}{2}}^{\frac{\pi}{2}} d\theta \frac{16\left(1 + |\Gamma_+|^2\right)\cos(\theta)^4 + 4Z^2\left(1 - |\Gamma_+\Gamma_-|^2\right)\cos(\theta)^2}{|4\cos(\theta)^2 + Z^2\left(1 - \Gamma_+\Gamma_-\right)|^2}, \tag{SE2}$$

where $\Gamma_\pm = \left(eV_2/|\Delta\left(\theta_\pm\right)|\right) - \sqrt{\left(eV_2/|\Delta\left(\theta_\pm\right)|\right) - 1}$ and $\theta_+ = \theta$, $\theta_- = \pi - \theta$. While $\Delta(\theta) = \Delta\cos\left[2\left(\theta - \alpha\right)\right]$ and α is the angle between the superconducting order parameter and the interface. The conductance $G_2\left(V_2\right)$ thus depends on the parameters α and on the BTK barrier strength Z. As discussed in the main text this block of the model leads to a proper description of the background conductance vs. the voltage bias.

Using $I = \int G\left(V\right) dV$ we obtain $G_1\left(I\right)$ and $G_2\left(I\right)$ and from these, we calculate the conductance when the two building blocks are connected in-series:

$$G\left(I\right) = \frac{1}{G_1(I)^{-1} + G_2(I)^{-1}} \tag{SE3}$$

Finally, using $V = \int \frac{1}{G(I)} dI$, we obtain $G(V)$.

II. SIMULATION PROCEDURE

In order to reproduce the experimental curves via simulations, we typically follow the procedure illustrated below. Blue curves are experimental data and orange curves correspond to the simulations. The examples in the following is is based on device A3D.

We first find Z and α that allow mimicking the conductance background. These parameters respectively characterize the YBCO/Au-graphene interface and the d-wave nature of the superconducting correlations.

Let us first assume that the normalized cavity length $\Lambda \to 0$ (so that there are no visible oscillations), fix $\alpha = 0$ and vary Z, the results are presented in the various panels of Fig. S1. We see that one needs relatively large $Z = 2$ to better reproduce the V-shaped "dip" around zero bias.

Now we explore the effect of varying α in Figs. S2 and S3. With these examples, one quickly realizes that it is not possible to use $\alpha \neq 0$ in the present case, regardless of the choice of Z, because $\alpha \neq 0$ yields to a sharp zero/bias conductance peak that is absent for this particular device.

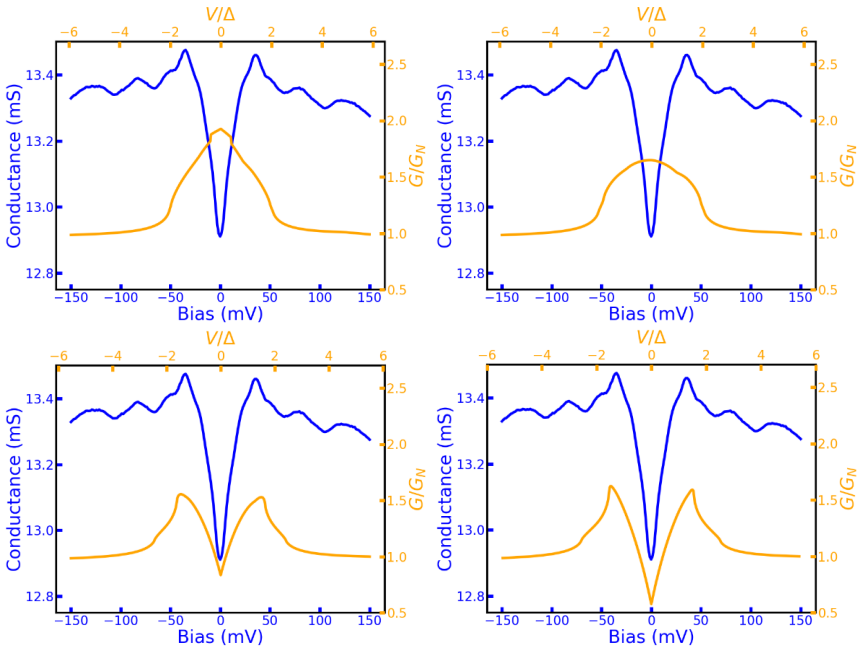

FIG. S1. Differential conductance experimental (blue) and theoretical (orange) as a function of the bias for $\Lambda \to 0$, $\alpha = 0$ and various values of the Z parameter: $Z = 0$ (top left), $Z = 0.5$ (top right), $Z = 1$ (bottom left) and $Z = 2$ (bottom right).

Considering the above, we would fix $Z = 2$ and $\alpha = 0$ for the A3D device.

Now we look for Λ and $\epsilon_{F,A}$ that yield oscillations of the same reduced period $\Delta V/\delta$ as in the experiments. We show in Figs. S4 and S5 some examples that illustrate how these parameters influence the oscillations period. First, we show examples with fixed $\epsilon_{F,A}$ and varying Λ (the red vertical lines mark minima in the experimental curve, allowing for a reference of experimental high-bias period): We see that increasing the cavity length Λ diminishes the oscillations period, as one would naturally expect. As shown in the Figs. S4 and S5, if one fixes Λ and varies $\epsilon_{F,A}$ the period is also modified, which is also expected. Indeed, from the definition of the parameters and the graphene's linear dispersion relation [3], the oscillations period is the same for any constant $\Lambda/\epsilon_{F,A}$. Note however that the choice of $\epsilon_{F,A}$ is not entirely free because this parameter modifies may introduce an asymmetry in the curve. Globally the

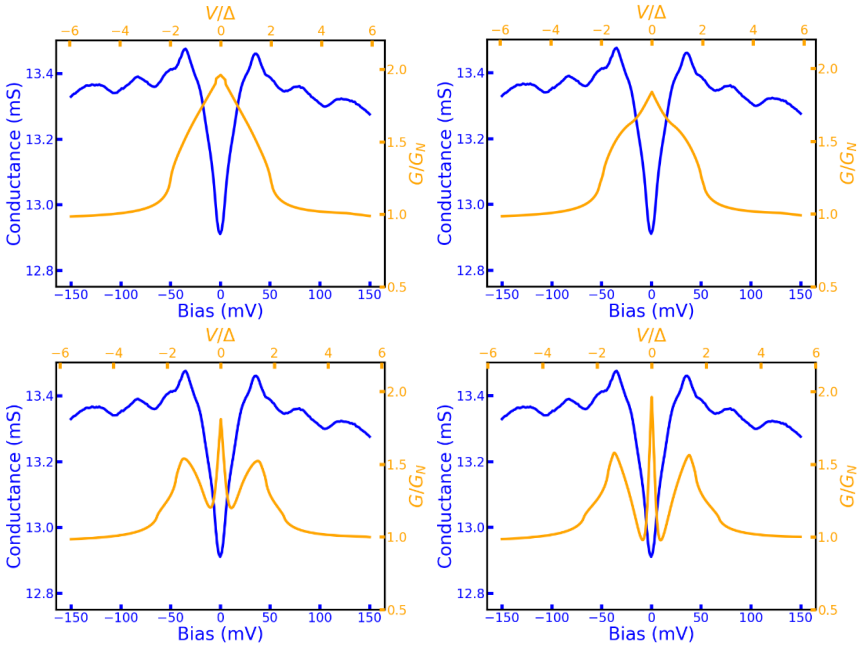

FIG. S2. Differential conductance experimental (blue) and theoretical (orange) as a function of the bias for $\alpha = 0.23$ and various values of the Z parameter: $Z = 0$ (top left), $Z = 0.5$ (top right), $Z = 1$ (bottom left) and $Z = 2$ (bottom right).

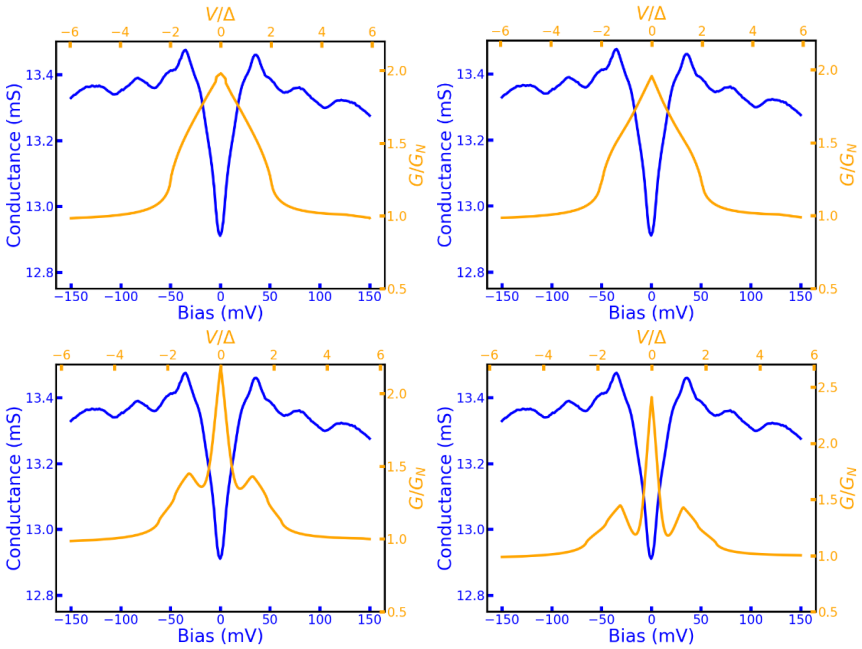

FIG. S3. Differential conductance experimental (blue) and theoretical (orange) as a function of the bias for $\alpha = 0.39$ and various values of the Z parameter: $Z = 0$ (top left), $Z = 0.5$ (top right), $Z = 1$ (bottom left) and $Z = 2$ (bottom right).

best agreement is found for the combination $\epsilon_{F,A} = 20$, $\Lambda = 10$.

Finally, $\epsilon_{F,B}$ and $\epsilon_{F,C}$ are adjusted in order to modulate the oscillations amplitude. As shown earlier for this model [3], the two latter parameters have no impact on the oscillations period, only on their amplitude and phase. This is because the Fermi velocity mismatch modifies the transmission/reflection across the interface. This is illustrated

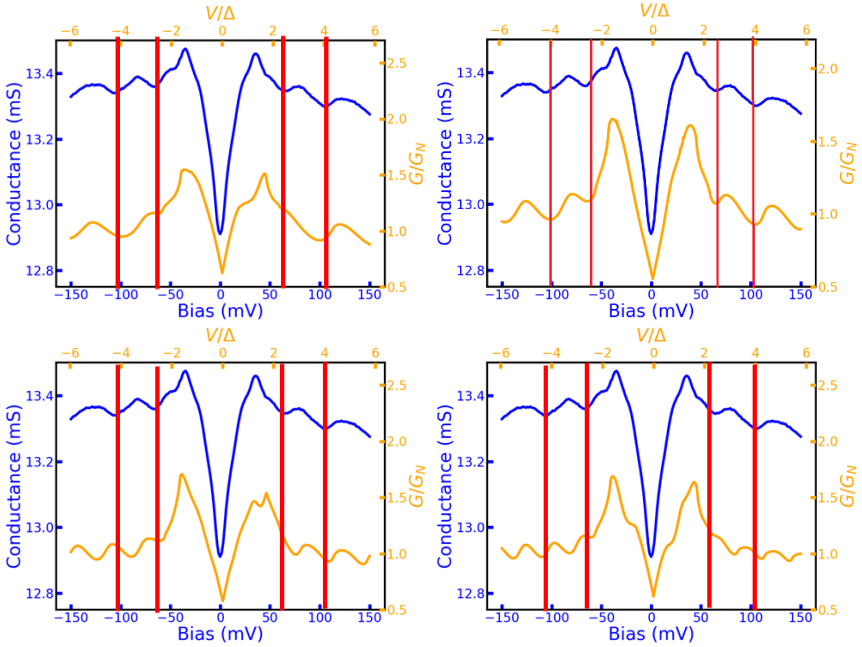

FIG. S4. Differential conductance experimental (blue) and theoretical (orange) as a function of the bias for $\epsilon_{F,A} = 20$ and various values of the Λ parameter: $\Lambda = 8$ (top left), $\Lambda = 10$ (top right), $\Lambda = 13$ (bottom left) and $\Lambda = 16$ (bottom right).

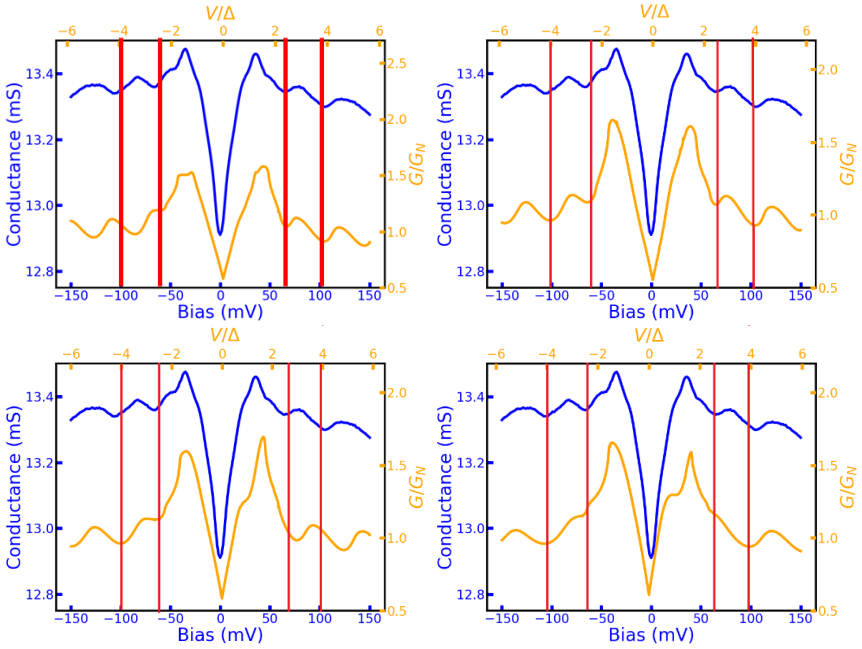

FIG. S5. Differential conductance experimental (blue) and theoretical (orange) as a function of the bias for $\Lambda = 10$ and various values of the $\epsilon_{F,A}$ parameter: $\epsilon_{F,A} = 18$ (top left), $\epsilon_{F,A} = 20$ (top right), $\epsilon_{F,A} = 22$ (bottom left) and $\epsilon_{F,A} = 25$ (bottom right).

in Figs. S6 and S7 where all the other parameters are kept constant at the optimum values deduced above.

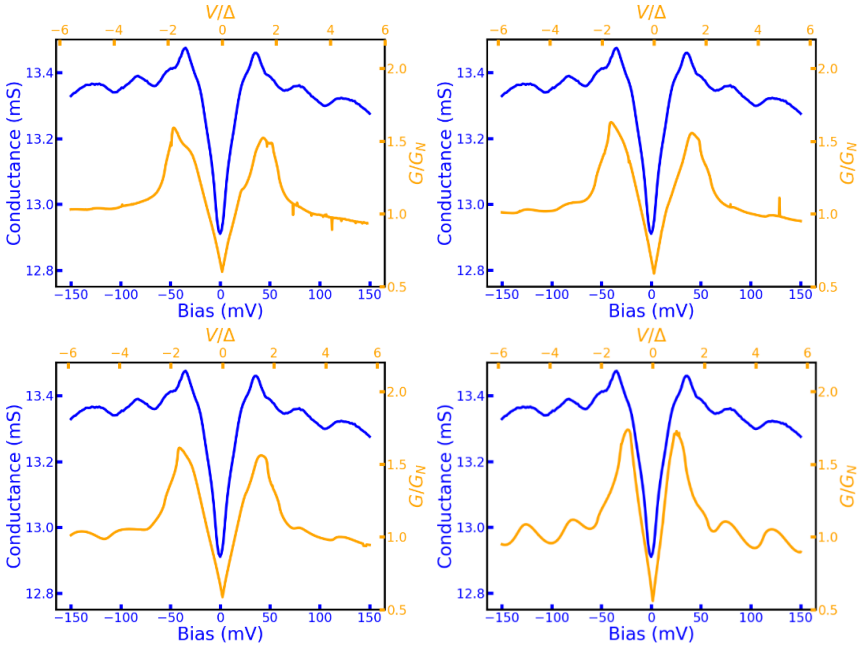

FIG. S6. Differential conductance experimental (blue) and theoretical (orange) as a function of the bias at the optimal parameter point and various values of the $\epsilon_{F,B}$ parameter: $\epsilon_{F,B} = 50$ (top left), $\epsilon_{F,B} = 100$ (top right), $\epsilon_{F,B} = 150$ (bottom left) and $\epsilon_{F,B} = 400$ (bottom right).

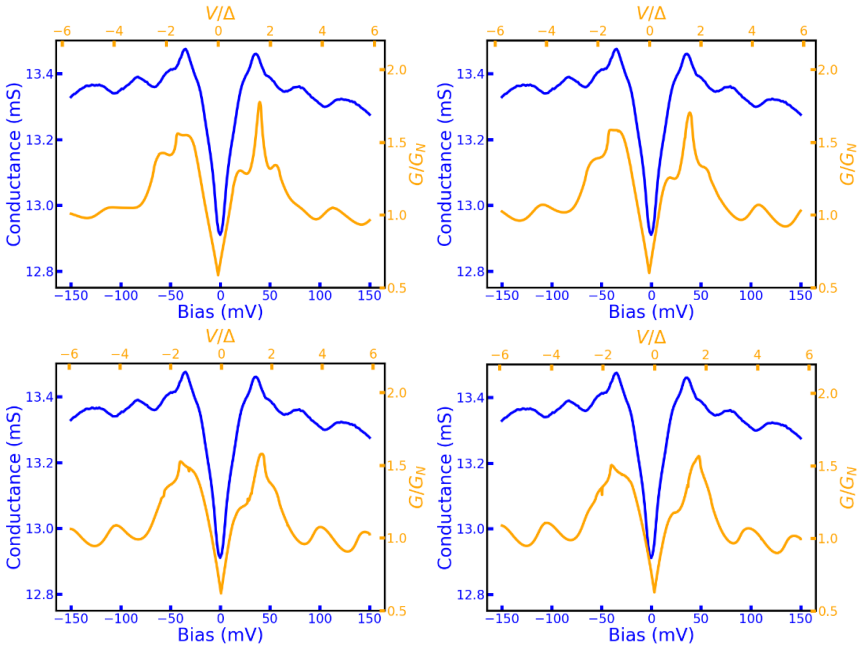

FIG. S7. Differential conductance experimental (blue) and theoretical (orange) as a function of the bias at the optimal parameter point and various values of the $\epsilon_{F,C}$ parameter: $\epsilon_{F,C} = 8$ (top left), $\epsilon_{F,C} = 12$ (top right), $\epsilon_{F,C} = 16$ (bottom left) and $\epsilon_{F,C} = 19$ (bottom right).

III. VARIABILITY OF THE FITTING PARAMETERS

In order to further illustrate the effect and variability of the key simulation parameters, we include below examples that show their impact on the simulations.

First examples: device, A5U. Best agreement simulation/experiment for $\epsilon_{F,A} = 14$, $Z = 0.25$, $\alpha = 0.39$, cf Fig. S8.

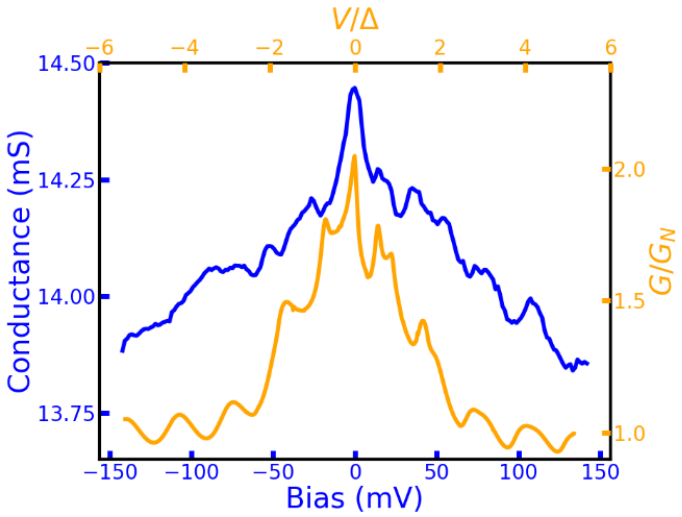

FIG. S8. Device **A5U**: Differential conductance experimental (blue) and theoretical (orange) as a function of the bias for $\epsilon_{F,A} = 14$, $Z = 0.25$, $\alpha = 0.39$.

Second example: device B3U. Best agreement for, $\epsilon_{F,A} = 20$, $Z = 1$, $\alpha = 0.008$, cf. Fig. S10.

From the these examples, one can see that the parameters can be typically varied $Z \pm 0.25$, $\alpha \pm 0.1$ and $\epsilon_{F,A} \pm 1$ before a significant change is observable in the simulations.

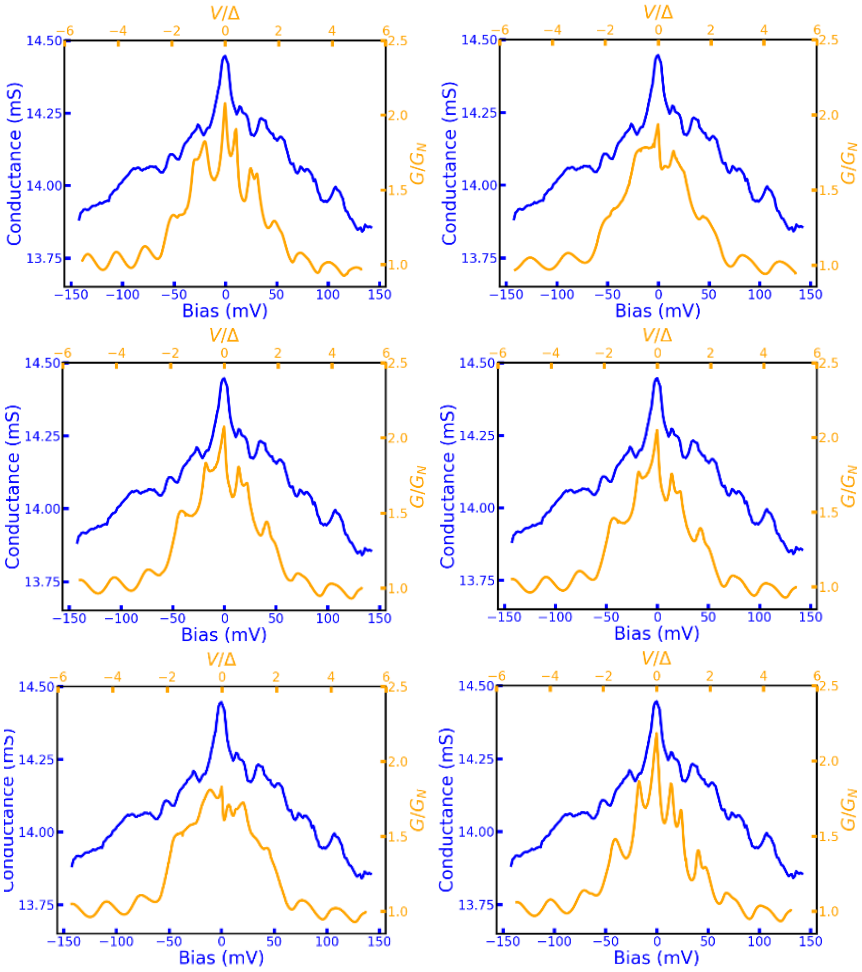

FIG. S9. Differential conductance experimental (blue) and theoretical (orange) as a function of the bias for different sets of fitting parameters: $\epsilon_{F,A} = 12$, $Z = 0.25$, $\alpha = 0.39$ (top left), $\epsilon_{F,A} = 16$, $Z = 0.25$, $\alpha = 0.39$ (top right), $\epsilon_{F,A} = 14$, $Z = 0$, $\alpha = 0.39$ (central left), $\epsilon_{F,A} = 14$, $Z = 0.5$, $\alpha = 0.39$ (central right), $\epsilon_{F,A} = 14$, Z=0.25, $\alpha = 0.23$ (bottom left), $\epsilon_{F,A} = 14$, $Z = 0.25$, $\alpha = 0.53$ (bottom right).

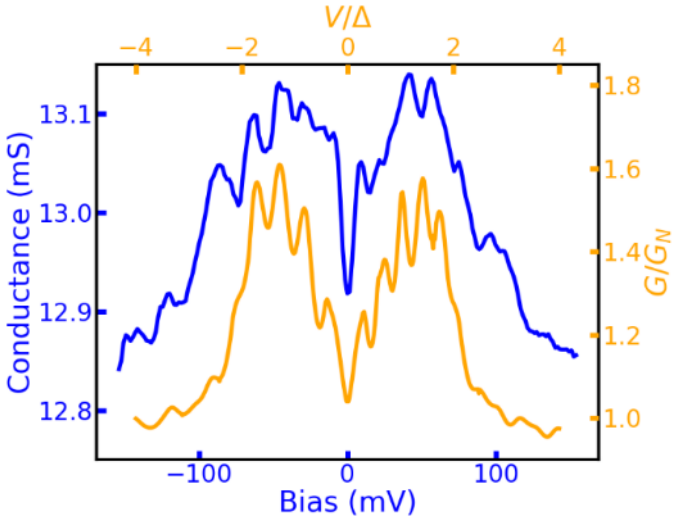

FIG. S10. Device **B3U**: Differential conductance experimental (blue) and theoretical (orange) as a function of the bias for $\epsilon_{F,A} = 20$, $Z = 1$, $\alpha = 0.008$.

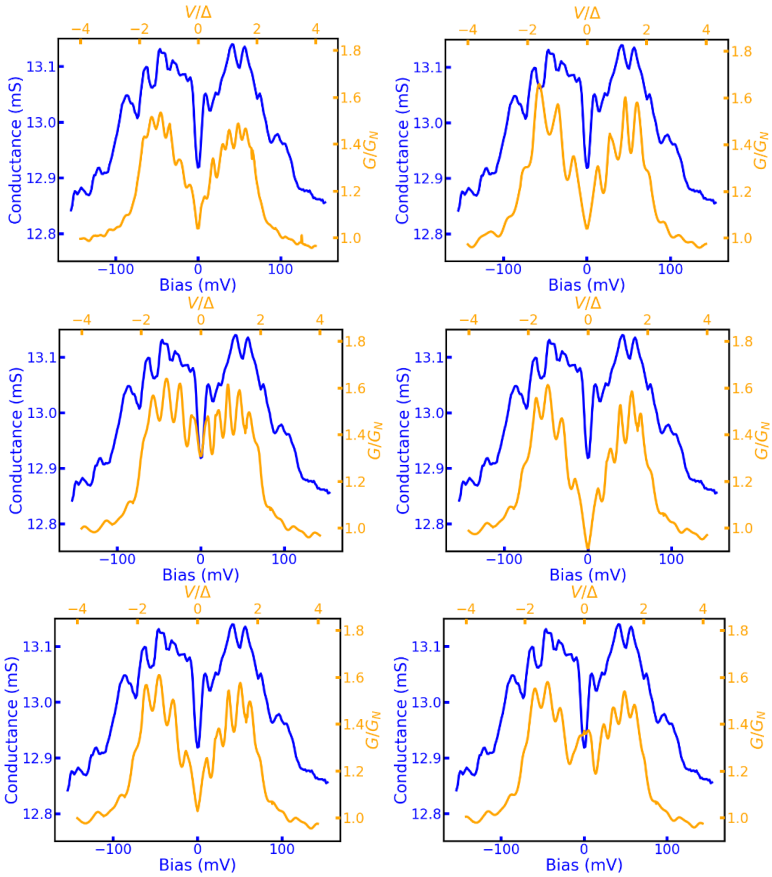

FIG. S11. Differential conductance experimental (blue) and theoretical (0.39) as a function of the bias for different sets of fitting parameters: $\epsilon_{F,A} = 15$, $Z = 1$, $\alpha = 0.008$ (top left), $\epsilon_{F,A} = 25$, $Z = 1$, $\alpha = 0.008$ (top right), $\epsilon_{F,A} = 20$, $Z = 0.7$, $\alpha = 0.008$ (central left), $\epsilon_{F,A} = 20$, $Z = 1.25$, $\alpha = 0.008$ (central right), $\epsilon_{F,A} = 20$, $Z = 1$, $\alpha = 0$ (bottom left), $\epsilon_{F,A} = 20$, $Z = 1$, $\alpha = 0.157$ (bottom right).

IV. QUANTITATIVE EVALUATION OF THE SIMULATION PARAMETERS

The simulations are based on dimensionless parameters whose values for each device are given in a table below. It is very important that their consistency can be quantitatively evaluated using fundamental relations and the actual device dimensions. As explained, above the two parameters that determine the oscillations period are Λ are $\epsilon_{F,A}$. Specifically, what defines the oscillations period is the ratio $\Lambda/\epsilon_{F,A}$.

If we take the definition of the parameters $\Lambda \equiv L/\lambda_{F,A}$ and $\epsilon_{F,A} \equiv E_{F,A}/\Delta$, and we consider the dispersion relationship in graphene $E_F = v_F k_F = h v_F/\lambda_F$ (with k_F and $v_F = 10^6$ m $\cdot$ s^{-1} the Fermi vector and velocity, and h the Planck constant), it is straightforward to find the following expression for the superconducting gap Δ:

$$\Delta = \left(\frac{\Lambda}{\epsilon_{F,A}}\right) h v_F L^{-1} \tag{SE4}$$

Equation (SE4) allows evaluating the simulations parameters quantitatively. If we input in Eq. (SE4) the actual graphene cavity length in the studied devices L_{device} (distance between YBCO electrodes defined lithographically) and the used $\frac{\Lambda}{\epsilon_{F,A}}$, we obtain a value for superconducting gap, which is similar for most of the devices varies between 15 meV and 20 meV. This is well within the values expected for the same YBCO films when moderately underdoped [5] and materials in proximity with YBCO [6].

That a strong proof of the consistency of the analysis, from the quantitative point of view.

V. TABLE OF SIMULATION PARAMETERS

Device	L_{device}	**Input parameters**						**Δ from Eq. SE4**
	nm	**Z**	α	Λ	$\epsilon_{F,A}$	$\epsilon_{F,B}$	$\epsilon_{F,C}$	meV
A3D	100	2	0	10	20	400	17.5	20.7
A3U	100	2	0	38	40	42.5	15.5	39.3
A5U	150	0.25	0.39	10	14	150	9.5	19.7
B3U	300	1	0.008	25	20	150	11.5	17.2
B4U	300	2	0	21	20	400	15	14.4
B4D	300	2.5	0.39	13	20	400	10	8.9
E3D	800	2.5	0.15	80	25	80	20	16.5

TABLE I. List of the fitting parameters for the devices analyzed.

VI. SIMULATION VS. EXPERIMENT FOR THE SET OF DEVICES

We present in the following the comparison between the experimental curves measured at 3.2 K (in blue) and the numerical simulation (in orange) based on the model detailed above.

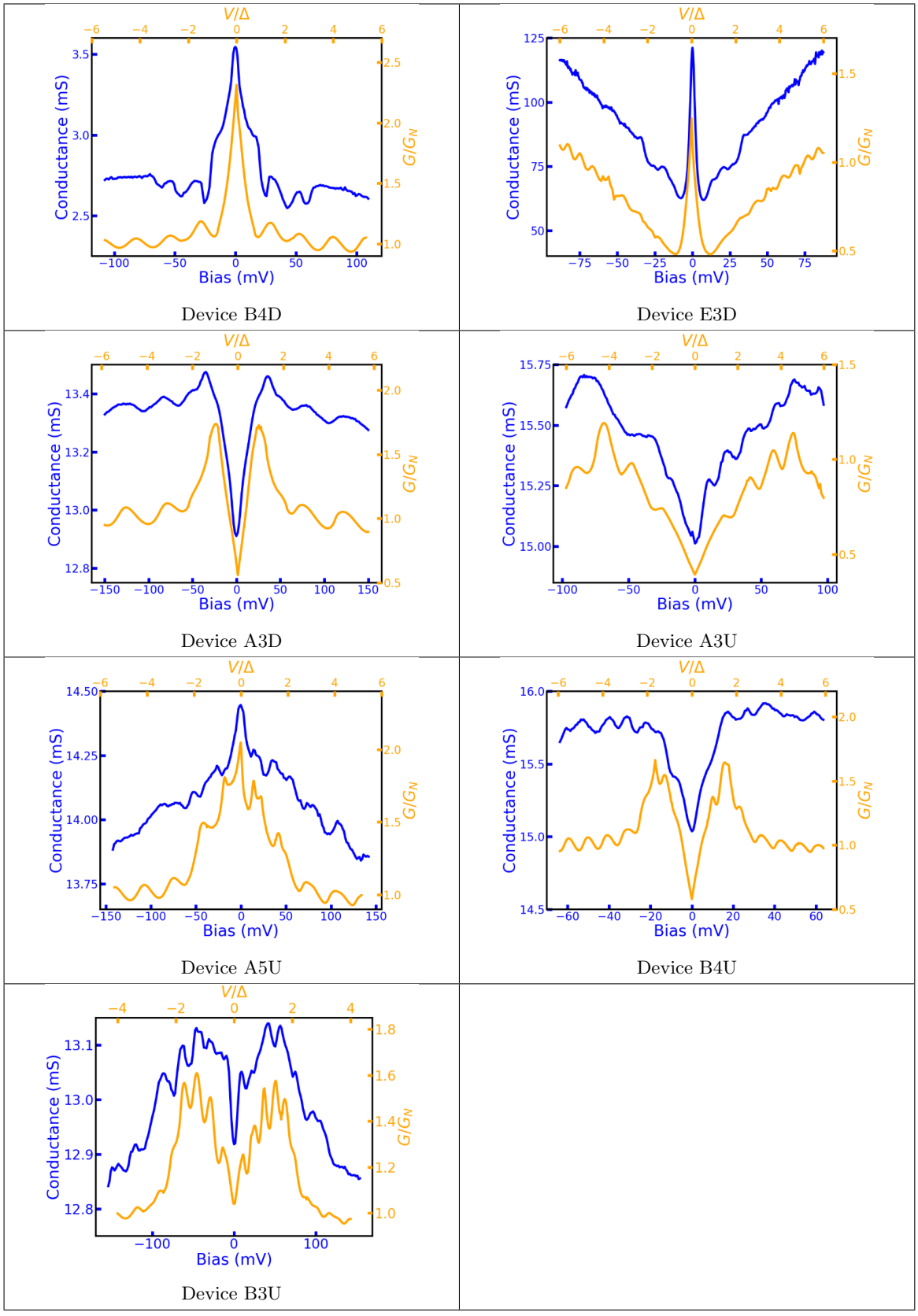

TABLE II. Comparison between the experimental curves measured at 3.2 K (in blue) and the numerical simulation (in orange) based on the model detailed above for all the devices analyzed.

VII. INDUCED SUPERCONDUCTING CORRELATIONS: d-WAVE VERSUS S-WAVE

In principle and accordingly to [7], we do not expect the Au layer to significantly disturb the d-wave pairing, because it is one order-of-magnitude thinner than the mean free path in this material.

In our experiments, the key evidence for the propagation of the d-wave correlations into graphene is the observation of spectral features that cannot be explained based on s-wave superconductivity. In particular, the sharp zero-bias peak in some others [Fig. 3(a) in the main text and devices E3D and B4D] are characteristic of d-wave junctions cannot be reproduced by the theoretical calculations unless one considers d-wave correlations in the proximitzed graphene homojunction.

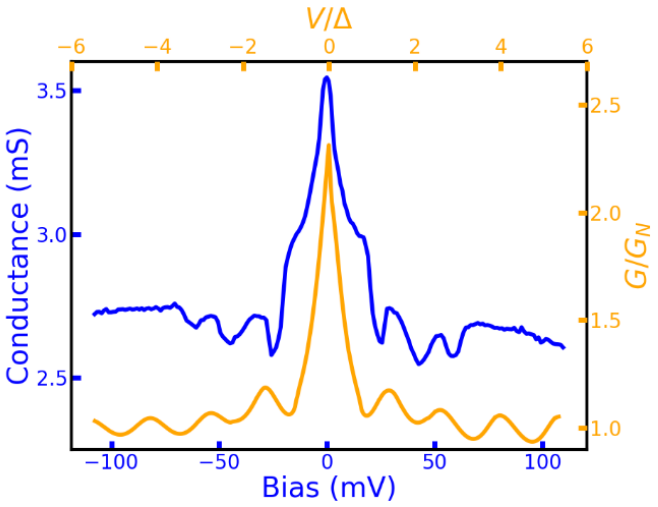

FIG. S12. Device **B4D**: Differential conductance experimental (blue) and theoretical (orange) as a function of the bias for $Z = 2.5$, $\alpha = 0.39$.

This is illustrated by the example shown in Fig. S12, which corresponds to device B4D. The best agreement between theory and experiment is obtained with a barrier strength $Z = 2.5$ and an effective angle between d-wave nodes and junction interfaces $\alpha = 0.39$.

In Fig. S13, we show simulations based on s-wave superconductivity both at the YBCO/Au-graphene interface and across the proximitized graphene homojunction. One can see that this assumption does not allow reproducing the experimental behaviour, particularly the sharp zero-bias conductance peak, even if the barrier strength Z is diminished to zero. Notice also that if the barrier strength Z is finite, a "dip" emerges around zero bias where s-wave quasiparticle tunnelling is strongly supressed. This is just opposite to the behaviour observed in the experiments.

Finally, we show in Fig. S14 simulations which consider d-wave superconductivity in the YBCO/Au-graphene interface and s-wave superconducting correlations across the graphene homojunction. One can see that under this assumption one cannot reproduce the behaviours observed experimentally.

The next example corresponds to device A5U, results in Fig. S15. We assume s-wave correlations across every junction interface. Again, the zero-bias conductance peak cannot be reproduced by considering only s-wave correlations-wave propagating the junction interfaces.

If we consider d-wave correlation only for the YBCO/Au-graphene interface and s-wave correlations across the

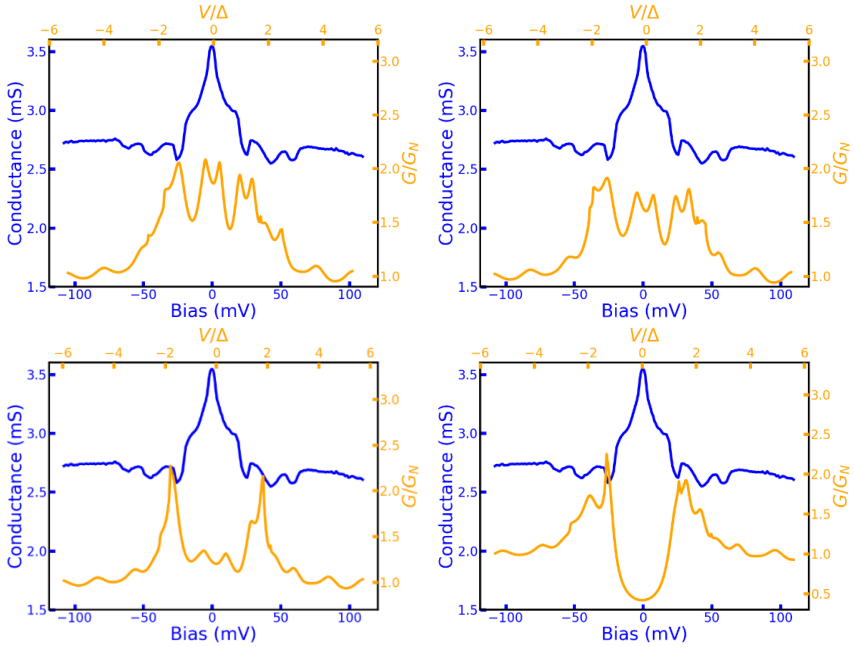

FIG. S13. Differential conductance experimental (blue) and theoretical (0.39) as a function of the bias for different sets of fitting parameters for the device B4D assuming a s-wave proximization: $Z = 1$ (top left), $Z = 0.5$ (top right), $Z = 1$ (bottom left), $Z = 2$ (bottom right).

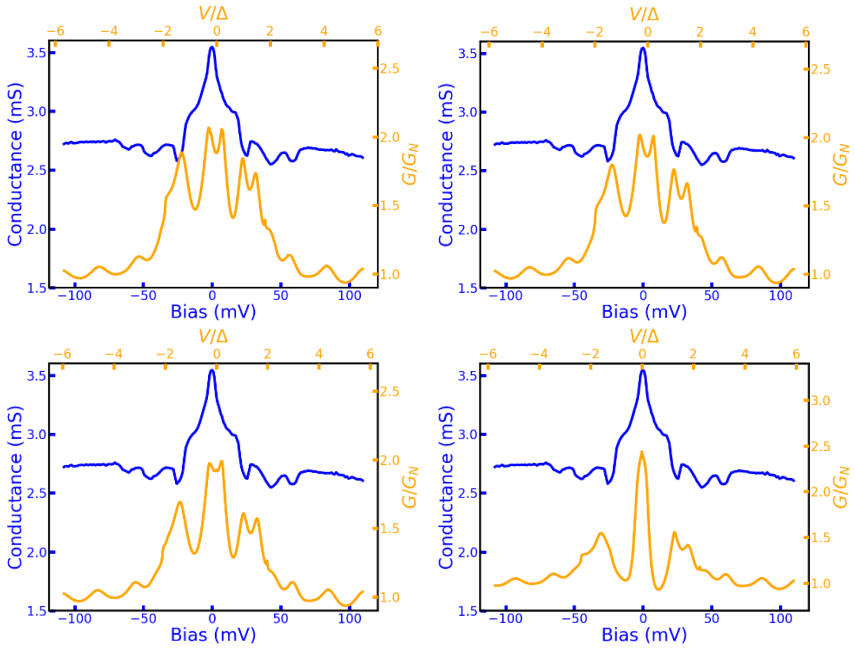

FIG. S14. Differential conductance experimental (blue) and theoretical (0.39) as a function of the bias for different sets of fitting parameters for the device B4D assuming a d-wave proximization: $Z = 1$ (top left), $Z = 0.5$ (top right), $Z = 1$ (bottom left), $Z = 2$ (bottom right).

homojunctions, the simulations do not allow reproducing the zero bias sharp zero bias conductance peak either, regardless of the barrier strength Z, see Fig. S16.

In summary, the experimental findings are well explained when it is assumed that d-wave superconducting correla-

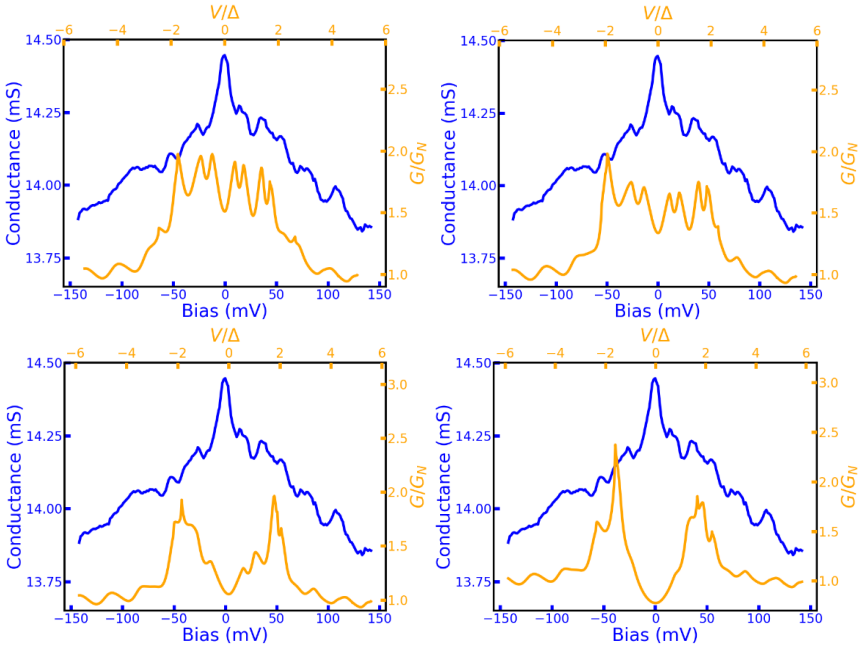

FIG. S15. Differential conductance experimental (blue) and theoretical (0.39) as a function of the bias for different sets of fitting parameters for the device A5U assuming a s-wave proximization: $Z = 1$ (top left), $Z = 0.5$ (top right), $Z = 1$ (bottom left), $Z = 2$ (bottom right).

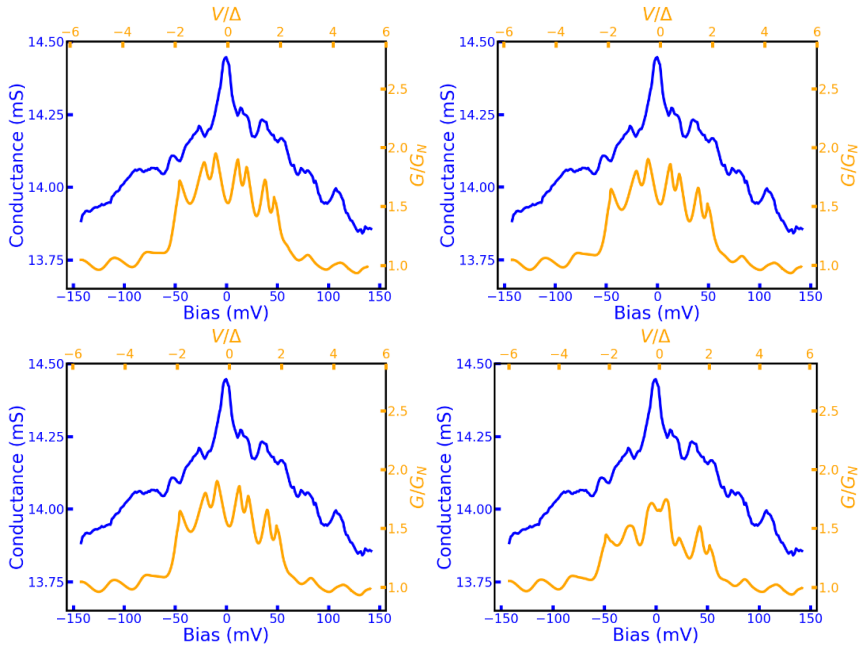

FIG. S16. Differential conductance experimental (blue) and theoretical (0.39) as a function of the bias for different sets of fitting parameters for the device A5U assuming a d-wave proximization: $Z = 1$ (top left), $Z = 0.5$ (top right), $Z = 1$ (bottom left), $Z = 2$ (bottom right).

tions propagate into the graphene homojunction, and exclude the s-wave pairing component.

Notice finally that the effective angle between the d-wave nodes and the junction interfaces changes randomly from device to device, which implies that it is not fixed by the device geometry. This suggests that the the contact between

the graphene and the superconducting electrodes might be inhomoegeneous and occur at edges of the SC electrodes or at exposed a-axis facets in the YBCO surface [6]. Local probes such as Scaning Tunneling microscopy would be necessary to investigate this question.

---

[1] J. Linder and A. Sudbø, Dirac fermions and conductance oscillations in s- and d-wave superconductor-graphene junctions, Phys. Rev. Lett. **99**, 147001 (2007).

[2] J. Y. T. Wei, N.-C. Yeh, D. F. Garrigus, and M. Strasik, Directional Tunneling and Andreev Reflection on $YBa_2Cu_3O_{7-\delta}$ Single Crystals: Predominance of d-Wave Pairing Symmetry Verified with the Generalized Blonder, Tinkham, and Klapwijk Theory, Phys. Rev. Lett. **81**, 2542 (1998).

[3] J. Linder and A. Sudbø, Tunneling conductance in s- and d-wave superconductor-graphene junctions: Extended Blonder-Tinkham-Klapwijk formalism, Phys. Rev. B **77**, 064507 (2008).

[4] D. Perconte, F. A. Cuellar, C. Moreau-Luchaire, M. Piquemal-Banci, R. Galceran, P. R. Kidambi, M.-B. Martin, S. Hofmann, R. Bernard, B. Dlubak, P. Seneor, and J. E. Villegas, Tunable Klein-like tunnelling of high-temperature superconducting pairs into graphene, Nature Physics **14**, 25 (2017).

[5] V. Rouco, R. El Hage, A. Sander, J. Grandal, K. Seurre, X. Palermo, J. Briatico, S. Collin, J. Trastoy, K. Bouzehouane, A. I. Buzdin, G. Singh, N. Bergeal, C. Feuillet-Palma, J. Lesueur, C. Leon, M. Varela, J. Santamaría, and J. E. Villegas, Quasiparticle tunnel electroresistance in superconducting junctions, Nature Communications **11**, 658 (2020).

[6] A. Sharoni, I. Asulin, G. Koren, and O. Millo, Proximity Effect in Gold-Coated $YBa_2Cu_3O_{7-\delta}$ Films Studied by Scanning Tunneling Spectroscopy, Phys. Rev. Lett. **92**, 017003 (2004).

[7] A. V. Balatsky, I. Vekhter, and J.-X. Zhu, Impurity-induced states in conventional and unconventional superconductors, Reviews of Modern Physics **78**, 373 (2006).